

Dual-domain Attention-based Deep Network for Sparse-view CT Artifact Reduction

Xiang Gao

Research Center for Medical Artificial Intelligence, Shenzhen Institute of Advanced Technology, Chinese Academy of Sciences, Shenzhen, Guangdong 518055, China
University of Chinese Academy of Sciences, Beijing 101408, China

Ting Su, Jiongtao Zhu & Jiecheng Yang

Research Center for Medical Artificial Intelligence, Shenzhen Institute of Advanced Technology, Chinese Academy of Sciences, Shenzhen, Guangdong 518055, China

Yunxin Zhang

Department of Vascular Surgery, Beijing Jishuitan Hospital, Beijing 100035, China

Donghua Mi

Department of Vascular Neurology, Beijing Tiantan Hospital, Capital Medical University, Beijing 100070, China

Hairong Zheng

Paul C Lauterbur Research Center for Biomedical Imaging, Shenzhen Institute of Advanced Technology, Chinese Academy of Sciences, Shenzhen 518055, China

Xiaojing Long, Dong Liang & Yongshuai Ge

Research Center for Medical Artificial Intelligence, Shenzhen Institute of Advanced Technology, Chinese Academy of Sciences, Shenzhen 518055, China

Paul C Lauterbur Research Center for Biomedical Imaging, Shenzhen Institute of Advanced Technology, Chinese Academy of Sciences, Shenzhen 518055, China

E-mail: ys.ge@siat.ac.cn

Abstract. Due to the wide applications of X-ray computed tomography (CT) in medical imaging activities, radiation exposure has become a major concern for public health. Sparse-view CT is a promising approach to reduce the radiation dose by down-sampling the total number of acquired projections. However, the CT images reconstructed by this sparse-view imaging approach suffer from severe streaking artifacts and structural information loss. In this work, an end-to-end dual-domain attention-based deep network (DDANet) is proposed to solve such an ill-posed CT image reconstruction problem. The image-domain CT image and the projection-domain sinogram are put into the two parallel sub-networks of the DDANet to independently extract the distinct high-level feature maps. In addition, a specified

attention module is introduced to fuse the aforementioned dual-domain feature maps to allow complementary optimizations of removing the streaking artifacts and mitigating the loss of structure. Numerical simulations, anthropomorphic thorax phantom and *in vivo* pre-clinical experiments are conducted to verify the sparse-view CT imaging performance of the DDANet. Results demonstrate that this newly developed approach is able to robustly remove the streaking artifacts while maintaining the fine structures. As a result, the DDANet provides a promising solution in achieving high quality sparse-view CT imaging.

1. INTRODUCTION

Over the past half century, computed tomography (CT) has witnessed an irreplaceable role in modern medical imaging applications. However, concerns about the risks of excessive radiation exposure have attracted a lot of attention. According to the International Commission on Radiological Protection (ICRP), every increase of 1 mSv radiation dose in human body would rise the chance of canceration by nearly 1/20000[1]. Nowadays, it has become a worldwide consensus to reduce the radiation dose of CT scans as low as reasonably achievable (ALARA). Dedicated researches from both the academic and industrial fields are performed to seek for the advanced low-dose CT imaging solutions .

Sparse-view CT scan is a promising approach to achieve low-dose CT imaging. By down-sampling the total number of the acquired projections, the radiation dose received by patients could be dramatically reduced. Different from the low-mAs scanning method[2, 3, 4], usually, the X-ray tube current over the sparse-view CT scan is not reduced. Thus, the CT images reconstructed from such dataset would not suffer from significant quantum noise issues. Whereas, the sparse-view CT images reconstructed from the conventional filtered back-projection (FBP) algorithm would contain dramatic streaking artifacts and loss of anatomical structure due to the data incompleteness. Therefore, improvement of the image quality in sparse-view CT imaging would be quite important for low-dose CT applications.

Over the past two decades, model-based iterative sparse-view CT image reconstruction methods were investigated by re-formulating the reconstruction task as a compression-aware optimization problem, in which certain prior information and mathematical optimization models are assumed to jointly remove the streaks. Because of the requirements of accurate forward model and parameter selections, the iterative CT reconstruction algorithms[5, 6, 7] may have limitations in generating high-quality CT images. Additionally, they may also have the drawback of long running time in certain applications.

Recently, the prosperity of the deep learning (DL) techniques unveils many opportunities in medical image reconstruction fields, and have demonstrated excellent performance in low-dose CT reconstruction. In the sparse-view CT imaging, majority of the previous studies focus on removing the streaking artifacts in the CT image domain.

For example, Jin et al.[8] applied the U-net, and Han et al.[9] proposed the dual frame U-net to perform sparse-view CT image reconstruction. Zhang et al.[10] proposed the DDNet to joint the advantages of Dense-net[11] and deconvolution operation. Kang et al.[12, 13] combined the wavelet transform, residual block[14] and CNN together to remove the streaks. As a contrary, the sinogram based networks can also be utilized. For example, the sparse-view sinogram is interpolated into the full-view one via the U-net in SSNet[15]. Li et al.[16] proposed the iCT-net to convert a sparse-view sinogram directly into a high-quality CT image. Lin et al.[17] decomposed the sparse-view inverse problem into a groups of simple transformations, and used a layered network to perform CT reconstructions.

Despite of the promising performance, one apparent limitation of the above CNN approaches is that they barely process the image-domain and the sinogram-domain information at the same time. Instead, only the single-domain information is considered and processed. To mitigate such drawback, recently, the dual-domain networks that are able to share mutual information have attracted many research interests. As in the CT imaging field, for instance, Wu et. al.[18] integrated a dual-domain (CT image domain and sinogram domain) sparse-view CT reconstruction network with the iterative reconstruction procedure, and Lin et al.[19] applied the dual-domain CNN to remove the metal artifacts.

Motivated by these aforementioned dual-domain studies, we herein propose a novel dual-domain attention deep network (DDANet) for high quality sparse-view CT reconstruction. In DDANet, a unique side-by-side network structure that ensures simultaneous feature extractions from the CT image and the sinogram is developed. Specifically, the U-Net is used to extract the features of CT images, the fully connected layer and atrous spatial pyramid pooling (ASPP)[20] module is used to extract the sinogram features, and the attention strategy is used to fuse the dual-domain features. The parallel feature extraction and high-level feature fusion allow information complement between the dual domains. The main contributions of this work are as follows:

- A novel side-by-side dual-domain network with a paralleled architecture is proposed. It shows outstanding performance in removing the sparse-view CT image artifacts.
- The attention mechanism is utilized to efficiently fuse the unique information learned from the sinogram domain and the CT image domain.
- The ASPP module with enlarged receptive field is employed to perform feature extractions in the sinogram domain.

2. METHOD

2.1. Problem Formulation

In this sparse-view CT artifact removal problem, there are two network inputs: the CT image $\mathbf{F} \in \mathbb{R}^{W_{img} \times H_{img} \times C_{img}}$ and the sinogram $\mathbf{S} \in \mathbb{R}^{W_{proj} \times H_{proj} \times C_{proj}}$. The network is

denoted as a function $g(\cdot)$. The goal of this work is to feed the F and S into $g(\cdot)$ to get the high-quality CT image $Q \in \mathbb{R}^{W_{img} \times H_{img} \times C_{img}}$ with mitigated streaking artifacts, namely:

$$Q = g(F, S) = \text{OP}_{\text{decode}}(\text{OP}_{\text{fusion}}(\text{OP}_F(F), \text{OP}_S(S))) \quad (1)$$

where OP_F represents the feature extraction operator of F , OP_S represents the feature extraction operator of S , $\text{OP}_{\text{fusion}}$ represents the feature fusion operator, and $\text{OP}_{\text{decode}}$ represents the feature decoding operator, see Fig. 1 and Fig. 2.

The overall structure of $g(\cdot)$ is shown in Fig. 1. It is a side-by-side dual-domain input network. The high-level sinogram information is extracted independently to assist the artifact removal in the CT image domain. The network output is a residual image, which is added back to the input FBP image to mitigate the sparse-view streaking artifacts. In addition, the attention-based feature fusion module, i.e., $\text{OP}_{\text{fusion}}$, is illustrated in Fig. 2.

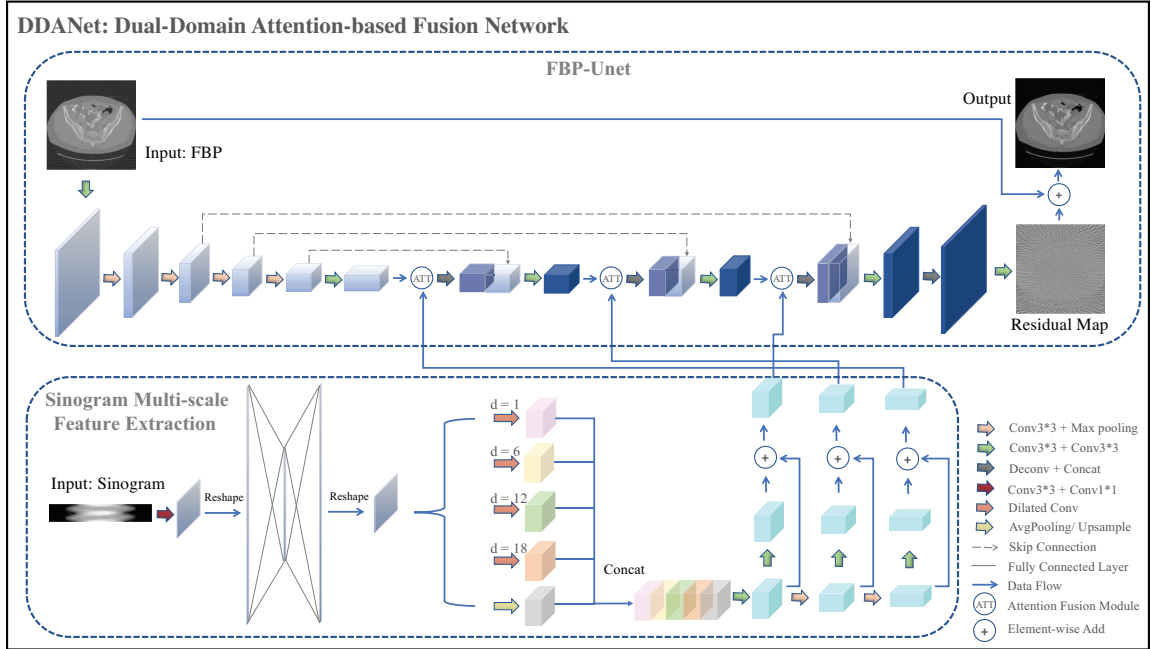


Figure 1: Architecture of the DDANet. Parameter d represents the dilation rate of the dilated convolution layer. Note that only the FBP-Unet module and the sinogram multi-scale feature extraction module are depicted.

2.2. FBP-Unet Module

This component corresponds to the OP_F operator in Eq. (1). The feature extractions are performed via the U-net[21]. In particular, feature maps with certain sizes (represented by $\{(w_1, h_1, c_1), (w_2, h_2, c_2), (w_3, h_3, c_3)\}$) of the CT images are obtained from each down-sampling stage. These features will be used for the subsequent feature fusions.

3. Sinogram Multi-scale Feature Extraction Module

This component corresponds to the OP_S operator in Eq. (1). By design, a fully connected layer is utilized to convert the sinogram onto the CT image domain. Different from the convolution, the fully connected layer is demonstrated to be more suitable for domain transformation [22]. In addition, a layer with fewer nodes is added as an intermediate layer to reduce the total number of parameters. Dilated convolutions with different rates ($d=1, d=6, d=12, d=18$) are applied to enlarge the areas of the receptive fields. In fact, the receptive field of a dilated convolution with a kernel size k_d and dilation rate d is equivalent to a convolution with a kernel size of k_c , namely,

$$k_c = k_d + (k_d - 1) * (d - 1) \quad (2)$$

Moreover, average pooling is also implemented. By doing so, the network receptive field can be easily expanded without significantly increasing the total number of network parameters. Next, the dilated feature maps and the pooled feature maps are concatenated and fed into the multi-scale sinogram features extraction network module. Correspondingly, three features with sizes of $\in \{(w_1, h_1, c_1), (w_2, h_2, c_2), (w_3, h_3, c_3)\}$ are extracted.

3.1. Attention-based Feature Fusion Module

This component corresponds to the OP_{fusion} operator in Eq. (1), and is denoted as ATT in Fig. 1. Specifically, a convolutional layer with a kernel size of 1×1 is used to extract the fused features \mathbf{I}_{fused} from the CT image feature \mathbf{I}_f and sinogram feature \mathbf{I}_s . The \mathbf{I}_f , \mathbf{I}_s and \mathbf{I}_{fused} belong to $\mathbb{R}^{W_i \times H_i \times C_i}$, where $W_i, H_i, C_i \in \{w, h, c | (w_1, h_1, c_1), (w_2, h_2, c_2), (w_3, h_3, c_3)\}$. Next, the plane attention module P_{att} , channel attention module D_{att} , and spatial attention module S_{att} are aggregated together to generate complete attention maps, which are multiplied with image-domain feature maps extracted from the FBP-Unet module, see more details in Fig. 2. As a result, certain spatial information that are beneficial for CT reconstruction are strengthened, and those irrelevant information are weakened.

Plane Attention Module extracts the plane feature map $M_p = [n_{1,1}, \dots, n_{1,H_i}, \dots, n_{W_i,1}, \dots, \dots, n_{W_i,H_i}] \in \mathbb{R}^{W_i \times H_i \times 1}$ via two convolutional layers. The sigmoid function is used to generate the final plane-attention map $\hat{M}_p = [\hat{n}_{1,1}, \dots, \hat{n}_{1,H_i}, \dots, \hat{n}_{W_i,1}, \dots, \hat{n}_{W_i,H_i}]$.

$$M_p = Conv_{7*7,1*1}(I_{fused}), \hat{M}_p = \sigma(M_p) \quad (3)$$

where $Conv$ denotes the convolutional layer, and σ denotes the sigmoid activation function. Afterwards, the \hat{M}_p is applied to the input FBP feature $\mathbf{I}_f = [p_{1,1}, \dots, p_{1,H_i}, \dots, p_{W_i,1}, \dots, p_{W_i,H_i}]$ with $p \in \mathbb{R}^{C_i}$ using plane-wise multiplication to obtain a feature map with different plane weights.

$$I_{fPA} = ATT_P(I_f, \hat{M}_p) = [p_{1,1}\hat{n}_{1,1}, \dots, p_{W_i,1}\hat{n}_{W_i,1}, \dots, p_{1,H_i}\hat{n}_{1,H_i}, \dots, p_{W_i,H_i}\hat{n}_{W_i,H_i}] \quad (4)$$

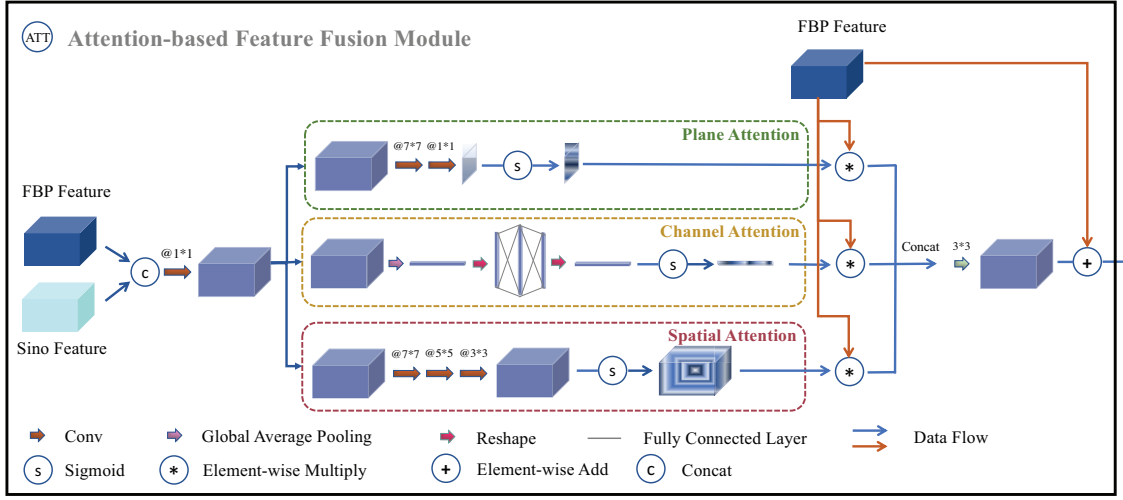


Figure 2: Structure of the attention-based feature fusion module. Three different attention mechanisms are used: plane attention, channel attention, and spatial attention.

Channel Attention Module squeezes the feature I_{fused} to obtain $M_c = [m_1, m_2, \dots, m_{C_i}] \in \mathbb{R}^{C_i}$ via a global average pooling of dimension $\mathbb{R}^{W_i \times H_i}$ and two fully connected layers. The M_c is activated by the sigmoid function to generate the channel-attention map $\hat{M}_c = [\hat{m}_1, \hat{m}_2, \dots, \hat{m}_{C_i}]$, namely,

$$M_c = fc(A(I_{fused})), \hat{M}_c = \sigma(M_c) \quad (5)$$

where fc denotes two fully connected layers with total node numbers of $C_i/2$ and C_i , A denotes the global average pooling, and σ denotes the sigmoid activation function. The \hat{M}_c is applied on the input CT feature $I_f = [c_1, c_2, \dots, c_{C_i}]$ with $c \in \mathbb{R}^{W_i \times H_i}$ using channel-wise multiplication to obtain a feature map with different channel weights.

$$I_{f_{CA}} = ATT_C(I_f, \hat{M}_c) = [c_1 \hat{m}_1, c_2 \hat{m}_2, \dots, c_{C_i} \hat{m}_{C_i}] \quad (6)$$

Spatial Attention Module enhances the level of attention. The spatial feature map $M_s = [z_{1,1,1}, \dots, z_{W_i, H_i, C_i}] \in \mathbb{R}^{W_i \times H_i \times C_i}$ is obtained from certain network convolution. The sigmoid activation function is used to generate the $\hat{M}_s = [\hat{z}_{1,1,1}, \dots, \hat{z}_{W_i, H_i, C_i}] \in \mathbb{R}^{W_i \times H_i \times C_i}$ map:

$$M_s = Conv_{7*7, 5*5, 3*3}(I_{fused}), \hat{M}_s = \sigma(M_s) \quad (7)$$

The \hat{M}_s is applied on the input CT feature $I_f = [s_{1,1,1}, \dots, s_{W_i, H_i, C_i}]$ with $s \in \mathbb{R}^1$ using channel-wise multiplication to obtain a feature map with different channel weights.

$$I_{f_{SA}} = ATT_S(I_f, \hat{M}_s) = [s_{1,1,1} \hat{z}_{1,1,1}, \dots, s_{W_i, H_i, C_i} \hat{z}_{W_i, H_i, C_i}] \quad (8)$$

Finally, these unique attention features obtained from the above three different attention modules are superimposed along the depth dimension, and convolution is used to fuse the complex information. As shown in Fig. 3, each attention map has a certain weight distribution.

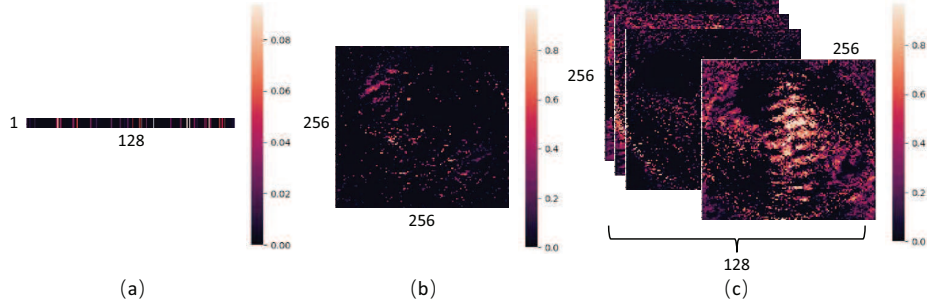


Figure 3: An example of the attention maps ($\in \mathbb{R}^{256 \times 256 \times 128}$) obtained from the proposed DDANet network: (a) the channel attention map, (b) the plane attention map, (c) the spatial attention map.

3.2. Network Training

3.2.1. Network Loss Function The network loss is a weighted summation of root-mean-square error (RMSE), structural similarity (SSIM) and peak signal-to-noise ratio (PSNR), see Eq. (9). Herein,

$$L_{loss} = \lambda_1 L_{rmse} + \frac{\lambda_2}{L_{ssim}} + \frac{\lambda_3}{L_{psnr}} \quad (9)$$

where λ_1 , λ_2 , and λ_3 present the corresponding weight, RMSE is used to control the global difference, SSIM is used to control the structural information, and PSNR is used to control the degree of noise.

3.2.2. Network Training Details The Adam optimizer was used, the initial learning rate was set to 1×10^{-4} with decay rate of 0.95 every epoch. The network training were performed on a single Nvidia RTX A4000 GPU card.

4. EXPERIMENTS

4.1. Dataset

4.1.1. Numerical data The data was prepared from the low dose CT images, which were published by the American Association of Physicists in Medicine (AAPM) low dose CT challenge[23]. The forward projections and CT image reconstructions were performed in Python with self-developed operators. Specifically, the distance from the X-ray source to the rotation center is 1000 mm, and is 1200 mm to the detector. There are 1024 detector elements with element of 0.6 mm \times 0.6 mm. The pixel size CT image is 0.625 mm \times 0.625 mm. In total, 5410 training data and 526 testing data were generated. By default, 128 sparse-view projections were simulated.

4.1.2. Experimental data Experimental data was acquired from an in-house CT imaging bench. The system was equipped with a rotating-anode X-ray tube (Varex G-242, Varex Imaging Corporation, UT, USA) and a flat panel detector (Varex

4343CB, Varex Image Corporation, UT, USA). The effective detector pixel size was $417\mu\text{m} \times 417\mu\text{m}$. The distance from the X-ray focal spot to the rotation center was 1156.3 mm, and was 1560.6 mm to the detector plane. The number of projections in the full-view CT scan was 900, with angular interval of 0.4 degree. The number of projections in the sparse-view CT scan was 128. An anthropomorphic thorax phantom (Model RS-111T, Radiology Support Devices, CA, USA) and an *in vivo* anaesthetized monkey were scanned. The animal experiment was performed in compliance with the protocol (SIAT-IACUC-201228-YGS-LXJ-A1498, 5 January 2021) that was approved by the Institutional Animal Care and Use Committee (IACUC) of the Shenzhen Institute of Advanced Technology at the Chinese Academy of Sciences.

4.1.3. Data enhancement The mixup[24] is used to augment the training data. Essentially, two individual images are mixed randomly over the network training with a certain weight:

$$\begin{aligned} F_{mixed} &= \lambda * F_1 + (1 - \lambda) * F_2 \\ S_{mixed} &= \lambda * S_1 + (1 - \lambda) * S_2 \\ G_{mixed} &= \lambda * G_1 + (1 - \lambda) * G_2 \end{aligned} \tag{10}$$

where λ denotes the weight coefficient sampled from the beta distribution. Symbols F, S and G denote the CT image, sinogram and the label, respectively. Every training data, has a 50% chance of being mixed up with the other one. One example of image mixup is shown in Figure 4. Be aware that the data mixup is not implemented on the test data.

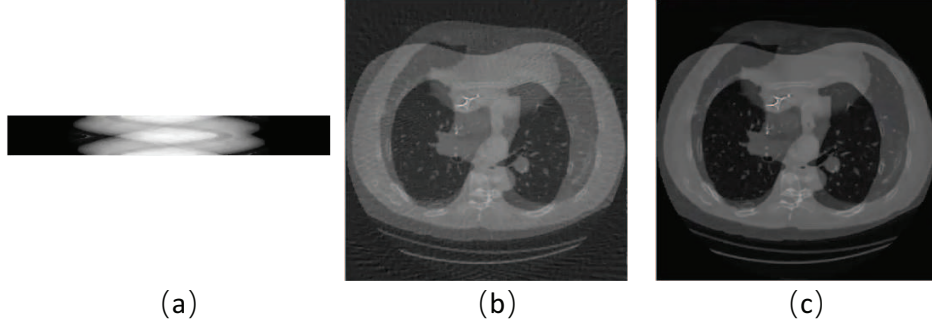


Figure 4: (a) Mixed sinogram with 128-view of projections, (b) mixed CT image reconstructed from (a), (c) ground truth of the mixed CT image in (b).

4.2. Ablation Experiments

Ablation experiments were performed to prove the effectiveness of the core modules of DDANet. The quantitative results are shown in Table 1. The baseline is the proposed DDANet without removing any module. In this case, RMSE is 4.2448×10^{-4} , SSIM is 0.9628, and PSNR is 42.7257.

4.2.1. Dual Domain The dual-domain input strategy, in which the sinogram domain information is used to assist the streaking artifact removals in the CT image domain, is implemented. However, it is still unclear whether the dual-domain strategy is necessary. To address this question, the sinogram-domain inputs is replaced by the CT image domain features. According to the results in Table 1, it is easy to see that the dual-domain inputs indeed greatly improve the network performance. One possible reason is that the information loss in CT image domain can be compensated by the sinogram domain feature.

4.2.2. Fully Connected Layer The fully connected layer in the sinogram feature extraction module was removed with the purpose to verify its effectiveness. All the other structures are kept unchanged. As seen in Table 1, the performance would be degraded compared to the DDANet. One possible explanation is that the sinogram and CT image contain different domain information, and the fully connected layer helps to perform the domain transformation and thus ease the fusion of different useful information, which are important for artifact removals.

4.2.3. Dilated Convolution The dilated convolution and the pooling operation (ASPP module) in the DDANet is removed to verify the effectiveness of the dilated convolution. As seen in Table 1, the DDANet without dilated convolution shows worse performance. One possible reason is that the streaking artifacts are global ones, and need to be mitigated via global operations. The dilated convolution exactly better takes this task than the conventional pooling and convolution operations.

4.2.4. Attention Fusion Module The output of DDANet is designed to be the streaking artifact only image, as a consequence, the attention fusion module plays the role of enhancing the extractions of streaking artifact feature information. As the results listed in the fourth and sixth rows of Table 1, clearly, the use of attention mechanism can boost the performance of DDANet in helping the intermediate layers be more focused

Table 1: Quantitative comparison results of the ablation experiments. The values of RMSE, PSNR and SSIM are estimated from the 526 test samples.

Network	Ablated Modules	Performance		
		RMSE	SSIM	PSNR
DDANet (Ablation)	Dual-Domain	4.5146×10^{-4}	0.9598	42.1833
	FC	4.3043×10^{-4}	0.9619	42.6036
	Dilated Conv	4.3349×10^{-4}	0.9617	42.5373
	Attention	4.4249×10^{-4}	0.9578	42.3586
	Mixup	4.3961×10^{-4}	0.9603	42.4156
DDANet	-	4.2448×10^{-4}	0.9628	42.7257

on extracting the artifact related features.

4.2.5. Mixup Data Augmentation Compared to the conventional data augmentation approaches such as image scaling and image rotation, the image mix-up can improve the model’s capability in capturing the artifacts distributions, and enhance its robustness to different object structures. As can be observed from Table 1, the training data mix-up results in an improvement of 0.1513×10^{-4} , 0.0025 and 0.3101 in RMSE, SSIM, and PSNR, respectively.

4.3. Comparison experiments

The TV[5], FBPCNet[8], RedCNN[25], DDNet[10], Frame Unet[9], SS-Net[15] methods are performed to compare with the DDANet. Essentially, these algorithms can be divided into three categories: the TV method belongs to the iterative algorithm, the FBPCNet, RedCNN, DDNet and Frame Unet methods represent the image-domain only post-processing strategy, and the SS-Net method represents the sinogram-domain only post-processing strategy.

5. RESULTS

5.1. Numerical results

The numerical performance of DDANet is validated on the AAPM low dose CT data, and results are presented in Fig. 5. As seen, the TV algorithm removes most of the streaking artifacts, but blurs the fine structures. The single-domain methods (including image-domain method and sinogram-domain method) have difficulty in removing substantial streaks while preserving fine details of the image. As a contrary, most of the streaks can be nicely removed by the developed DDANet without sacrificing the image sharpness.

Table 2: Quantitative comparison results for the 128-view CT imaging. The averaged performance of the 526 testing images and the performance of the two selected cases in Fig. 5 are evaluated.

Type	Method	Group Mean			Case #1			Case #2		
		RMSE	SSIM	PSNR	RMSE	SSIM	PSNR	RMSE	SSIM	PSNR
		(10 ⁻⁴)			(10 ⁻⁴)			(10 ⁻⁴)		
Analytical	FBP	15.374	0.5836	31.5229	11.412	0.6094	31.5333	12.762	0.5250	29.5876
Image-Domain	Iterative	TV[5]	4.6465	0.9541	41.9347	3.5378	0.9423	40.6055	3.2527	0.9429
		FBPCovNet[8]	4.7517	0.9544	41.7357	3.5552	0.9402	40.1832	3.0470	0.9489
		RedCNN[25]	5.1121	0.9459	41.0911	3.6973	0.9327	39.6745	3.2117	0.9388
		DDNet[10]	4.7141	0.9545	41.8076	3.5760	0.9402	40.2092	3.0476	0.9493
		Frame Unet[9]	4.6920	0.9554	41.8470	3.6032	0.9411	40.2065	3.1123	0.9494
Sinogram-Domain	SS-Net[15]	7.6899	0.9033	37.5562	5.3517	0.8819	36.4759	4.7687	0.8945	
Dual-Domain	DDANet	4.2448	0.9628	42.7257	3.2861	0.9482	40.8635	2.7069	0.9596	41.2300

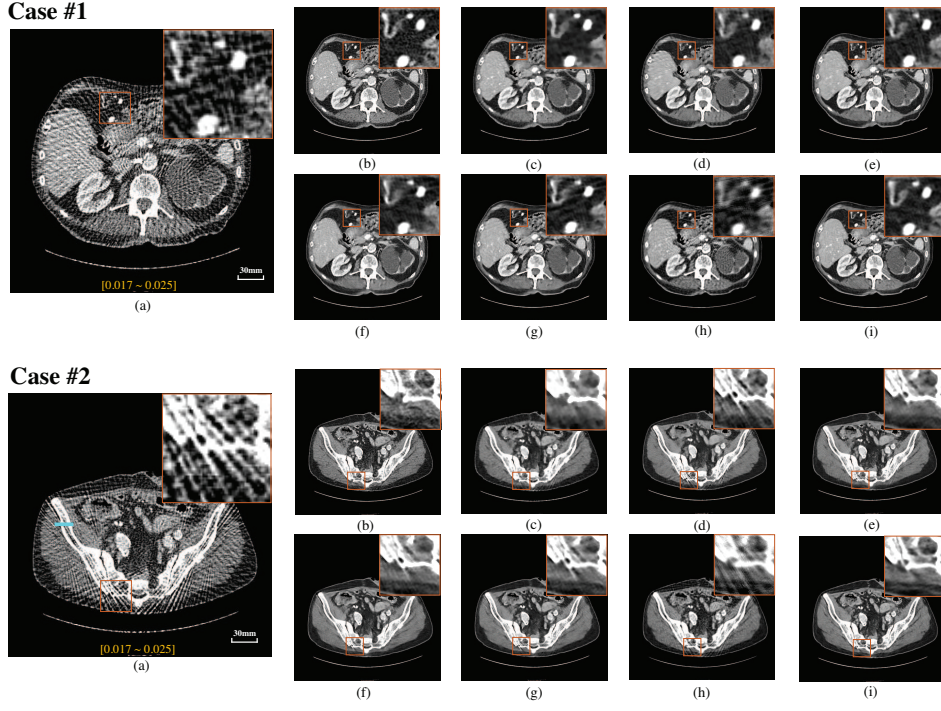


Figure 5: Results of simulated CT images for different reconstruction methods: (a) FBP, (b) Ground truth, (c) TV, (d) RedCNN, (e) FBPCNN, (f) Frame Unet, (g) DDNet, (h) SS-Net, (i) DDANet. The display window is $[0.017, 0.025] \text{ mm}^{-1}$. The scale-bar denotes 30 mm.

In addition, line profiles of the high-contrast bone (highlighted in blue in Fig. 5(a), Case #2) were also compared, see Fig. 6. It is observed that the DDANet method generates the most consistent profile comparing to the ground truth, indicating the best capability of maintaining the signal precision and image sharpness. The quantitative analysis results are listed in Table 2. Again, the DDANet achieves the smallest RMSE value, and the highest SSIM and PSNR values.

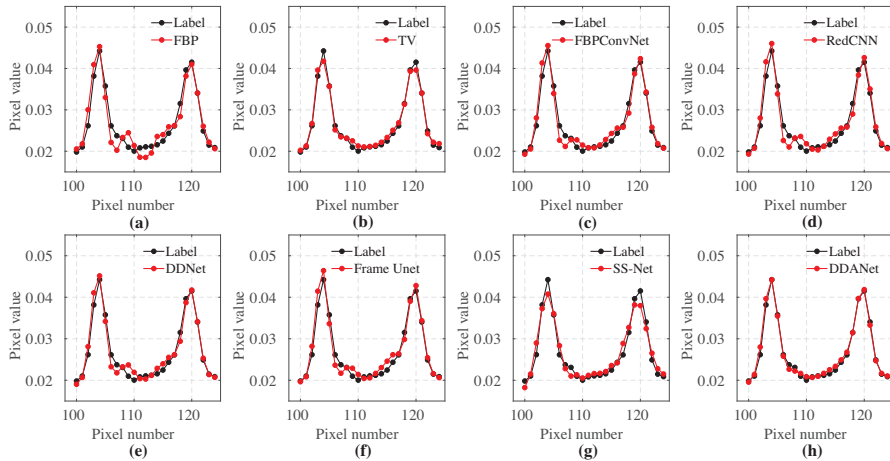


Figure 6: The profiles along the horizontal green line in Fig. 5(a) (Case #2). The red curves denote the ground truth, and the blue curves denote the different methods: (a) FBP, (b) TV, (c) RedCNN, (d) FBPCNN, (e) Frame Unet, (f) DDNet, (g) SS-Net, (h) DDANet.

5.2. Results of robustness study

The robustness of the proposed DDANet network in removing the streaking artifacts over different sparse-view projection data, i.e., 64, 256, 384 and 512, are investigated, see the results in Fig. 7. As observed, the image quality gets less satisfactory when the number of projections is 64. However, DDANet is still able to remove most of the streaking artifacts and keep the majority of structural information intact under this very challenging condition. As the number of projections increases, the quality of the reconstructed CT images from DDANet boosts gradually, and the residual losses are found to be negligible. Additionally, the quantitative analysis results are listed in Table 3. Be aware that certain convolutions and pooling layers are altered in the sinogram feature extraction module for those sinograms with different dimensions (not equal to 128) to keep consistent feature sizes.

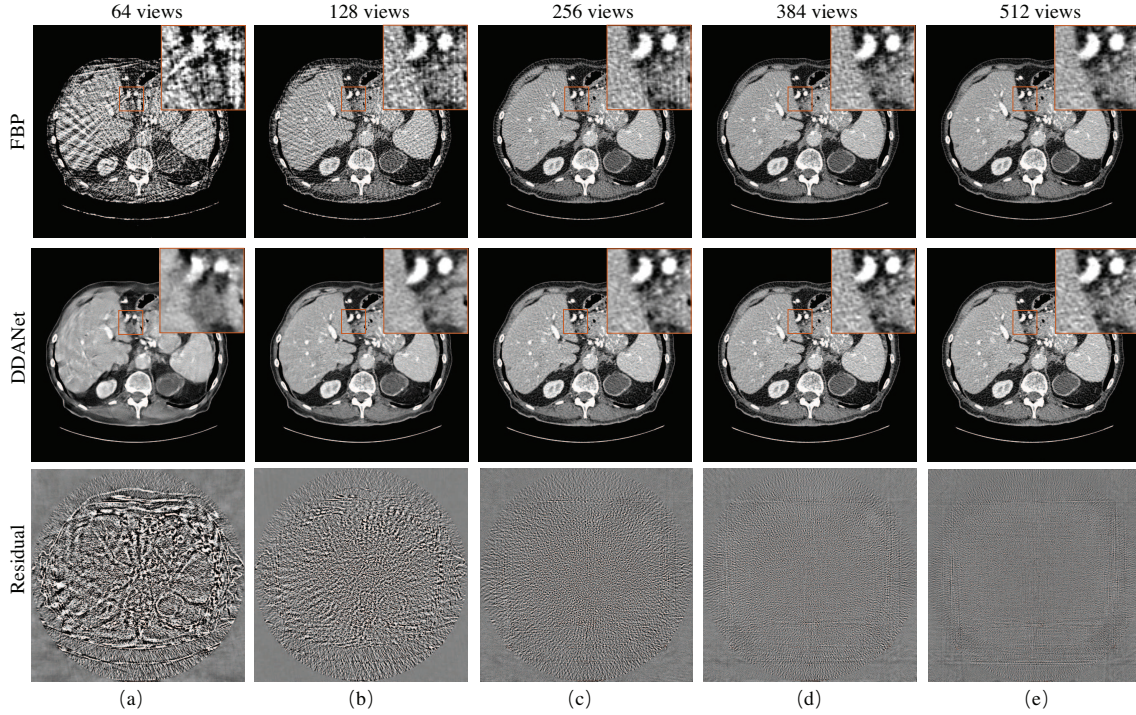


Figure 7: Results of different number of projections. Images in the first row are reconstructed by the FBP algorithm, and images in the second row are reconstructed by the DDANet. The residual images of the ground truth and DDANet are depicted in the third row. The display window is $[0.017, 0.025]$ mm^{-1} for the CT images, and $[-0.001, 0.001]$ mm^{-1} for the residual images.

5.3. Experimental results

Two experimental sparse-view CT imaging data, an anthropomorphic thorax phantom and an anaesthetized monkey, are verified, see the results in Fig. 8 and Fig. 9. With regard to the selected region-of-interest (ROI) in Fig. 8, it can be seen that the proposed DDANet outperforms the other methods in removing the streaking artifacts. Although

Table 3: Quantitative comparison results for different views (68, 128, 256, 384, 512).

Views	FBP / DDANet		
	RMSE (10^{-4})	SSIM	PSNR
64	27.801 / 6.7533	0.3741 / 0.9297	26.3721 / 38.6759
128	15.374 / 4.2448	0.5836 / 0.9628	31.5229 / 42.7257
256	7.9227 / 3.1028	0.8343 / 0.9762	37.2751 / 45.4483
384	4.6774 / 2.3546	0.9338 / 0.9857	41.8533 / 47.8435
512	3.6605 / 1.8875	0.9590 / 0.9893	43.9816 / 49.7658

the TV and FrameUnet methods are able to reduce more artifacts, the reconstructed images become quite blurry. For the animal experiments, again, the DDANet shows the best capability in eliminating the streaking artifacts, see the regions highlighted by the white arrows in Fig. 9.

Moreover, the image spatial resolution, i.e., the modulation transfer function (MTF), is compared quantitatively, see the plots in Fig. 10. Specifically, the MTF curves are calculated from the highlighted bone/tissue region (cyan line) in Fig. 8. Overall, the MTF curves further confirm the visual performance in Fig. 8 and Fig. 9. For example, the MTF curve generated from the TV algorithm gets narrower, indicating a certain loss of the image resolution. Compared with the reference FBP method (for full-view reconstruction), the DDANet method slightly degrades the image resolution. Note that the MTF is measured on the high-contrast object, thus the actual visual performance may get varied for low-contrast objects.

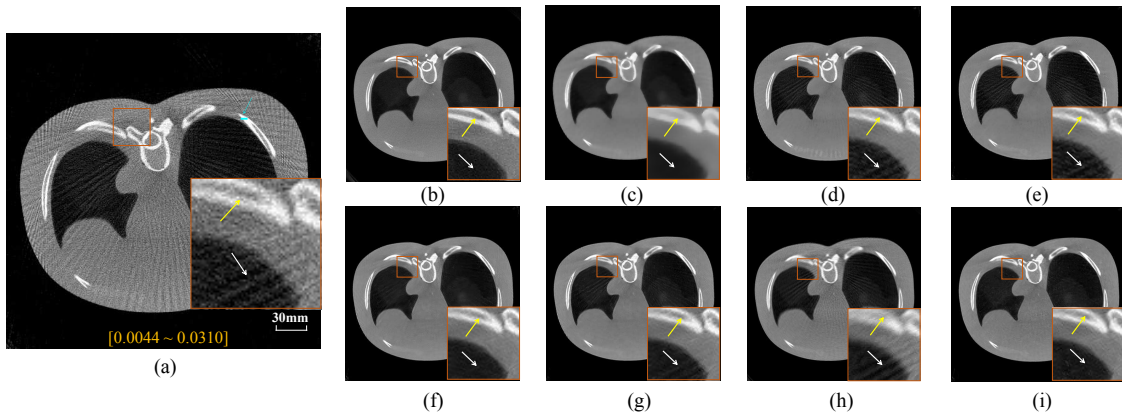


Figure 8: Experimental results of the thorax phantom: (a) FBP, (b) Ground truth, (c) TV, (d) RedCNN, (e) FBPCNN, (f) FrameUnet, (g) DDANet, (h) SS-Net, (i) DDANet. The display window is $[0.004, 0.031] \text{ mm}^{-1}$. The scale-bar denotes 30 mm.

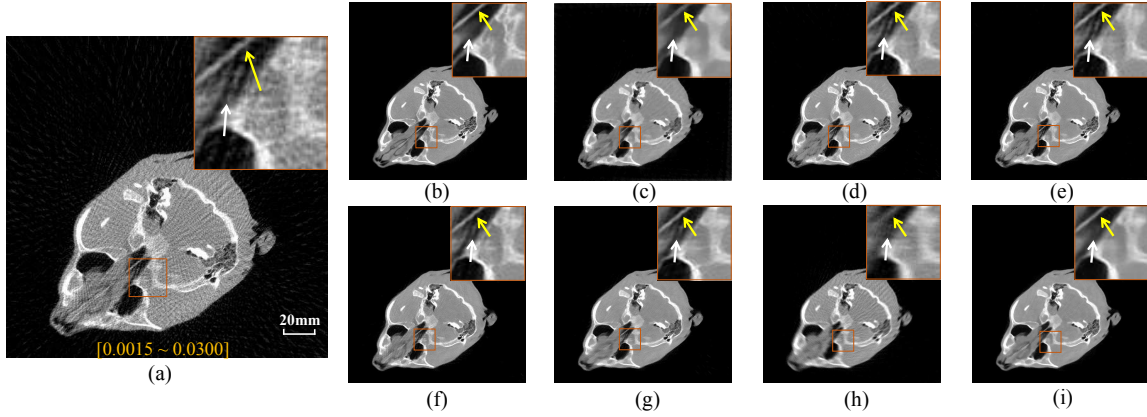


Figure 9: Experimental results of the monkey head: (a) FBP, (b) Ground truth, (c) TV, (d) RedCNN, (e) FBPCNN, (f) FrameUNet, (g) DDNet, (h) SS-Net, (i) DDANet. The display window is $[0.001, 0.030] \text{ mm}^{-1}$. The scale-bar denotes 20 mm.

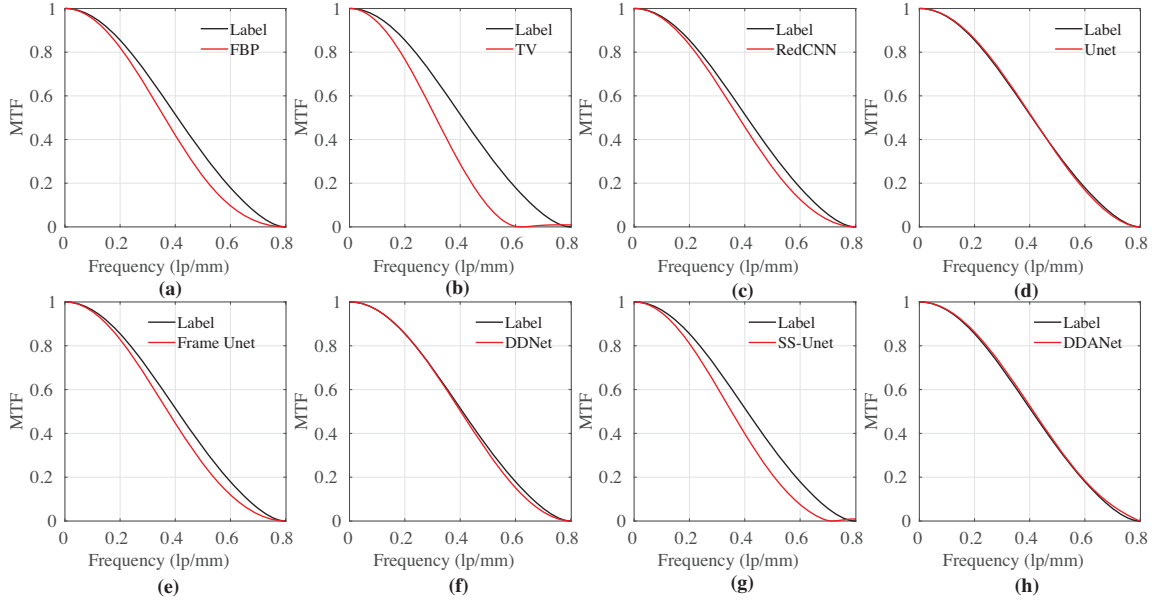


Figure 10: The MTF results. (a) FBP, (b) TV, (c) RedCNN, (d) FBPCNN, (e) Frame UNet, (f) DDNet, (g) SS-Net, (h) DDANet.

6. DISCUSSION AND CONCLUSION

In this work, a dual-domain attention network (DDANet) is proposed for the sparse-view CT imaging. Different from the reconstruction methods developed based on the single-domain information, DDANet is able to simultaneously utilize the dual-domain (CT image domain and sinogram domain) information. With such a particular network design, additional mutual information could be accessed to assist the sparse-view CT image reconstructions. To generate the best imaging performance, certain techniques are used to enhance the feature extractions. For instance, the fully connected layer is adopted to perform domain transformation between the sinogram and the CT image, the

dilated convolutional layer is utilized to enlarge the receptive field, multiple attention mechanisms are incorporated to make feature fusions. The superior performance of the DDANet network are verified via additional ablation experiments. Finally, numerical simulations, phantom and animal experiments are conducted. Results demonstrate the advancement of the dual-domain based DDANet in reducing the streaking artifacts for sparse-view CT imaging.

The trained DDANet by numerical data is directly used on the experimental data without any network fine tuning. Due to this reason, the reconstructed experimental CT images may show inferior performance than the numerical simulations. Enhanced performance of the DDANet network would be expected if further network fine tuning could be implemented on real experimental data.

In future, the following topics can be investigated: (1) the self-attention mechanism defined in the transformer network[26] could be used to carry out the global feature extractions, particularly for the sinogram-domain sub-network. By doing so, the removal of the streaking artifacts that spread over the entire CT image could become more effective. (2) the hint learning[27] approach would be tested and incorporated to replace the fully connected layer in the sinogram-domain sub-network with the purpose of greatly shrinking the total size of the network parameters while minimally degrading the entire network performance.

In conclusion, a dedicated end-to-end dual-domain attention-based deep network (DDANet) is proposed to reconstruct high quality sparse-view CT images. The performance of DDANet is validated on the numerical simulations, anthropomorphic thorax phantom and *in vivo* preclinical experiments. Results demonstrate that this newly developed network is able to remove the streaking artifacts robustly while maintaining the fine structural details in sparse-view low-dose CT imaging.

ACKNOWLEDGMENT

The authors would like to thank Dr. Yaoqin Xie for borrowing the anthropomorphic thorax phantom. This work is supported by Guangdong Basic and Applied Basic Research Foundation (2019A1515011262, 2020A1515110685), Shenzhen Basic Research Program (Grant No. JCYJ20200109115212546), Guangdong Key Area Research Program (2020B1111130001), National Natural Science Foundation of China (12027812, 11804356), Youth Innovation Promotion Association of Chinese Academy of Sciences (2021362).

References

- [1] H Smith. *1990 recommendations of the International Commission on Radiologic al Protection*, volume 21(1-3). International Commission on Radiological Protection, 1991.
- [2] J. Gu and J. C. Ye. Adain-based tunable cyclegan for efficient unsupervised low-dose ct denoising. *IEEE Transactions on Computational Imaging*, PP(99):1–1, 2021.

- [3] Kaichao Liang, Li Zhang, Yirong Yang, Hongkai Yang, and Yuxiang Xing. A self-supervised deep learning network for low-dose ct reconstruction. In *2018 IEEE Nuclear Science Symposium and Medical Imaging Conference (NSS/MIC)*, volume PP, pages 1–4, 2018.
- [4] Qiaoqiao Ding, Yuesong Nan, Hao Gao, and Hui Ji. Deep learning with adaptive hyper-parameters for low-dose ct image reconstruction. *IEEE Transactions on Computational Imaging*, 7:648–660, 2021.
- [5] Weiwen Wu, Dianlin Hu, Kang An, Shaoyu Wang, and Fulin Luo. A high-quality photon-counting ct technique based on weight adaptive total-variation and image-spectral tensor factorization for small animals imaging. *IEEE Transactions on Instrumentation and Measurement*, 70:1–14, 2020.
- [6] Qiong Xu, Hengyong Yu, Xuanqin Mou, Lei Zhang, Jiang Hsieh, and Ge Wang. Low-dose x-ray ct reconstruction via dictionary learning. *IEEE transactions on medical imaging*, 31(9):1682–1697, 2012.
- [7] Hua Zhang, Jing Huang, J. Ma, Zhaoying Bian, and Wufan Chen. Iterative reconstruction for x-ray computed tomography using prior-image induced nonlocal regularization. *IEEE transactions on bio-medical engineering*, 61(9), 2014.
- [8] K. H. Jin, M. T. Mccann, E. Froustey, and M. Unser. Deep convolutional neural network for inverse problems in imaging. *IEEE Transactions on Image Processing*, PP(99):4509–4522, 2016.
- [9] Y. Han and J. C. Ye. Framing u-net via deep convolutional framelets: Application to sparse-view ct. *IEEE Transactions on Medical Imaging*, page 1418, 2018.
- [10] Z. Zhang, X. Liang, D. Xu, Y. Xie, and G. Cao. A sparse-view ct reconstruction method based on combination of densenet and deconvolution. *IEEE Transactions on Medical Imaging*, 37(6):1–1, 2018.
- [11] Gao Huang, Zhuang Liu, Laurens Van Der Maaten, and Kilian Q Weinberger. Densely connected convolutional networks. pages 4700–4708, 2017.
- [12] Eunhee Kang, Junhong Min, and Jong Chul Ye. A deep convolutional neural network using directional wavelets for low-dose x-ray ct reconstruction. *Medical physics*, 44(10):e360–e375, 2017.
- [13] Eunhee Kang, Jong Chul Ye, et al. Wavelet domain residual network (wavresnet) for low-dose x-ray ct reconstruction. *arXiv preprint arXiv:1703.01383*, 2017.
- [14] Kaiming He, Xiangyu Zhang, Shaoqing Ren, and Jian Sun. Deep residual learning for image recognition. In *Proceedings of the IEEE conference on computer vision and pattern recognition*, pages 770–778, 2016.
- [15] L. Hyeon, L. Jongha, K. Hyeonseok, C. Byungchul, and C. Seungryong. Deep-neural-network based sinogram synthesis for sparse-view ct image reconstruction. *IEEE Transactions on Radiation & Plasma Medical Sciences*, pages 1–1, 2018.
- [16] Y. Li, K. Li, C. Zhang, J. C. Montoya, and G. H. Chen. Learning to reconstruct computed tomography (ct) images directly from sinogram data under a variety of data acquisition conditions. *IEEE Transactions on Medical Imaging*, PP(99), 2019.
- [17] Lin Fu and Bruno De Man. A hierarchical approach to deep learning and its application to tomographic reconstruction. In *15th International Meeting on Fully Three-Dimensional Image Reconstruction in Radiology and Nuclear Medicine*, volume 11072, page 1107202. International Society for Optics and Photonics, 2019.
- [18] W Wu, D Hu, C Niu, H Yu, V Vardhanabhuti, and G Wang. Drone: Dual-domain residual-based optimization network for sparse-view ct reconstruction. *IEEE Transactions on Medical Imaging*, 40:3002–3014, 2021.
- [19] Wei-An Lin, Haofu Liao, Cheng Peng, Xiaohang Sun, Jingdan Zhang, Jiebo Luo, Rama Chellappa, and Shaohua Kevin Zhou. Dudonet: Dual domain network for ct metal artifact reduction. In *2019 IEEE/CVF Conference on Computer Vision and Pattern Recognition (CVPR)*, pages 10504–10513, 2019.
- [20] Liang-Chieh Chen, Yukun Zhu, George Papandreou, Florian Schroff, and Hartwig Adam.

- Encoder-decoder with atrous separable convolution for semantic image segmentation. In *Proceedings of the European conference on computer vision (EC CV)*, pages 801–818, 2018.
- [21] Olaf Ronneberger, Philipp Fischer, and Thomas Brox. U-net: Convolutional networks for biomedical image segmentation. pages 234–241, 2015.
- [22] Bo Zhu, Jeremiah Z Liu, Stephen F Cauley, Bruce R Rosen, and Matthew S Rosen. Image reconstruction by domain-transform manifold learning. *Nature*, 555(7697):487–492, 2018.
- [23] Aapm. (2017). low dose ct grand challenge. [online]. available: <http://www.aapm.org/grandchallenge/lowdosect/#>.
- [24] Hongyi Zhang, Moustapha Cisse, Yann N Dauphin, and David Lopez-Paz. mixup: Beyond empirical risk minimization. *arXiv preprint arXiv:1710.09412*, 2017.
- [25] C. Hu, Z. Yi, M. K. Kalra, L. Feng, C. Yang, P. Liao, J. Zhou, and W. Ge. Low-dose ct with a residual encoder-decoder convolutional neural network (red-cnn). *IEEE Transactions on Medical Imaging*, 36(99):2524–2535, 2017.
- [26] Ashish Vaswani, Noam Shazeer, Niki Parmar, Jakob Uszkoreit, Llion Jones, Aidan N Gomez, Lukasz Kaiser, and Illia Polosukhin. Attention is all you need. In *Advances in neural information processing systems*, pages 5998–6008, 2017.
- [27] Adriana Romero, Nicolas Ballas, Antoine Kahou, Samira Ebrahimi and Chassang, Carlo Gatta, and Yoshua Bengio. Fitnets: Hints for thin deep nets. *arXiv preprint arXiv:1412.6550*, 2014.